Design and comparison of GaAs, GaAsP and InGaAlAs quantum-well active regions for 808-nm VCSELs

Yan Zhang,[1,2] Yongqiang Ning,[1,*] Lisen Zhang,[1,2] Jinsheng Zhang,[1,2] Jianwei Zhang,[1,2] Zhenfu Wang,[1,2] Jian Zhang,[1,2] Yugang Zeng,[1] and Lijun Wang[1]

[1]*Key Laboratory of Excited State Processes, Changchun Institute of Optics, Fine Mechanics and Physics, Jilin Changchun, 130033, China*

[2]*Graduate University of Chinese Academy of Sciences, Beijing, 100039, China*

**ningyq@ciomp.ac.cn*

Abstract: Vertical-cavity surface-emitting lasers emitting at 808 nm with unstrained $GaAs/Al_{0.3}Ga_{0.7}As$, tensilely strained $GaAs_xP_{1-x}/Al_{0.3}Ga_{0.7}As$ and compressively strained $In_{1-x-y}Ga_xAl_yAs/Al_{0.3}Ga_{0.7}As$ quantum-well active regions have been investigated. A comprehensive model is presented to determine the composition and width of these quantum wells. The numerical simulation shows that the gain peak wavelength is near 800 nm at room temperature for GaAs well with width of 4 nm, $GaAs_{0.87}P_{0.13}$ well with width of 13 nm and $In_{0.14}Ga_{0.74}Al_{0.12}As$ well with width of 6 nm. Furthermore, the output characteristics of the three designed quantum-well VCSELs are studied and compared. The results indicate that $In_{0.14}Ga_{0.74}Al_{0.12}As$ is the most appropriate candidate for the quantum well of 808-nm VCSELs.

©2011 Optical Society of America

OCIS codes: (140.7260) Vertical cavity surface emitting lasers; (140.3070) Infrared and far-infrared lasers; (160.3380) Laser materials; (270.3430) Laser theory.

References and links

1. A. Valle, M. Sciamanna, and K. Panajotov, "Nonlinear dynamics of the polarization of multitransverse mode vertical-cavity surface-emitting lasers under current modulation," Phys. Rev. E Stat. Nonlin. Soft Matter Phys. **76**(4), 046206 (2007).
2. Y. Ding, W. Fan, D. Xu, C. Tong, Y. Liu, and L. Zhao, "Low threshold current density, low resistance oxide-confined VCSEL fabricated by a dielectric-free approach," Appl. Phys. B **98**(4), 773–778 (2010).
3. L. A. D'Asaro, J. F. Seurin, and J. D. Wynn, "High-power, high-efficiency VCSELs pursue the goal," Photon. Spectra **39**, 62–66 (2005).
4. E. Hugues-Salas, R. P. Giddings, X. Q. Jin, J. L. Wei, X. Zheng, Y. Hong, C. Shu, and J. M. Tang, "Real-time experimental demonstration of low-cost VCSEL intensity-modulated 11.25 Gb/s optical OFDM signal transmission over 25 km PON systems," Opt. Express **19**(4), 2979–2988 (2011).
5. Z. Wang, Y. Ning, Y. Zhang, J. Shi, X. Zhang, L. Zhang, W. Wang, D. Liu, Y. Hu, H. Cong, L. Qin, Y. Liu, and L. Wang, "High power and good beam quality of two-dimensional VCSEL array with integrated GaAs microlens array," Opt. Express **18**(23), 23900–23905 (2010).
6. J.-F. Seurin, C. L. Ghosh, V. Khalfin, A. Miglo, G. Xu, J. D. Wynn, P. Pradhan, and L. A. D'Asaro, "High-power high-efficiency 2D VCSEL arrays," Proc. SPIE **6908**, 690808 (2008).
7. J. Sakaguchi, T. Katayama, and H. Kawaguchi, "All-optical memory operation of 980-nm polarization bistable VCSEL for 20-Gb/s PRBS RZ and 40-Gb/s NRZ data signals," Opt. Express **18**(12), 12362–12370 (2010).
8. K. Iga, "Vertical-cavity surface-emitting laser: Its conception and evolution," Jpn. J. Appl. Phys. **47**(1), 1–10 (2008).
9. Y. K. Kuo, J. R. Chen, M. L. Chen, and B. T. Liou, "Numerical study on strained InGaAsP/InGaP quantum wells for 850-nm vertical-cavity surface-emitting lasers," Appl. Phys. B **86**(4), 623–631 (2007).
10. L. Mutter, B. Dwir, A. Caliman, V. Iakovlev, A. Mereuta, A. Sirbu, and E. Kapon, "Intra-cavity patterning for mode control in 1.3 μm coupled VCSEL arrays," Opt. Express **19**(6), 4827–4832 (2011).
11. A. Hurtado, A. Quirce, A. Valle, L. Pesquera, and M. J. Adams, "Nonlinear dynamics induced by parallel and orthogonal optical injection in 1550 nm Vertical-Cavity Surface-Emitting Lasers (VCSELs)," Opt. Express **18**(9), 9423–9428 (2010).
12. J.-F. Seurin, G. Xu, V. Khalfin, A. Miglo, J. D. Wynn, P. Pradhan, C. L. Ghosh, and L. A. D'Asaro, "Progress in high-power high-efficiency VCSEL arrays," Proc. SPIE **7229**, 722903 (2009).

#146072 - $15.00 USD Received 18 Apr 2011; accepted 1 Jun 2011; published 14 Jun 2011

13. L. Goldberg, C. McIntosh, and B. Cole, “VCSEL end-pumped passively Q-switched Nd:YAG laser with adjustable pulse energy,” Opt. Express **19**(5), 4261–4267 (2011).
14. M. Grabherr, M. Miller, R. Jaeger, D. Wiedenmann, and R. King, “Commercial VCSELs reach 0.1 W cw output power,” Proc. SPIE **5364**, 174–182 (2004).
15. Y.-Q. Hao, Y. Luo, Y. Feng, C.-L. Yan, Y.-J. Zhao, Y.-X. Wang, X.-H. Wang, Y. Qu, and G.-J. Liu, “Large aperture vertical cavity surface emitting laser with distributed-ring contact,” Appl. Opt. **50**(7), 1034–1037 (2011).
16. PICS3D by Crosslight Software, Inc., Burnaby, Canada, 2005, http://www.crosslight.com.
17. J. Minch, S. H. Park, T. Keating, and S. L. Chuang, “Theory and experiment of $In_{1-x}Ga_xAs_yP_{1-y}$ and $In_{1-x-y}Ga_xAl_yAs$ long-wavelength strained quantum-well lasers,” IEEE J. Quantum Electron. **35**(5), 771–782 (1999).
18. C. G. Van de Walle, “Band lineups and deformation potentials in the model-solid theory,” Phys. Rev. B Condens. Matter **39**(3), 1871–1883 (1989).
19. S. Adachi, *Properties of Semiconductor Alloys: Group-IV, III–V and II–VI Semiconductors* (Wiley, 2009).
20. C. Chih-Sheng and C. Shun Lien, “Modeling of strained quantum-well lasers with spin-orbit coupling,” IEEE J. Sel. Top. Quantum Electron. **1**(2), 218–229 (1995).
21. P. Zhang, Y. Song, J. Tian, X. Zhang, and Z. Zhang, “Gain characteristics of the InGaAs strained quantum wells with GaAs, AlGaAs, and GaAsP barriers in vertical-external-cavity surface-emitting lasers,” J. Appl. Phys. **105**(5), 053103 (2009).
22. J. W. Matthews and A. E. Blakeslee, “Defects in epitaxial multilayers: I. Misfit dislocations,” J. Cryst. Growth **27**, 118–125 (1974).
23. S. F. Yu, *Analysis and Design of Vertical Cavity Surface Emitting Lasers* (Wiley-Interscience, 2003).
24. H. Soda, Y. Motegi, and K. Iga, “GaInAsP/InP surface emitting injection lasers with short cavity length,” IEEE J. Quantum Electron. **19**(6), 1035–1041 (1983).
25. K. Iga, F. Koyama, and S. Kinoshita, “Surface emitting semiconductor lasers,” IEEE J. Quantum Electron. **24**(9), 1845–1855 (1988).
26. B. Lu, P. Zhou, J. Cheng, K. J. Malloy, and J. C. Zolper, “High temperature pulsed and continuous-wave operation and thermally stable threshold characteristics of vertical-cavity surface-emitting lasers grown by metalorganic chemical vapor deposition,” Appl. Phys. Lett. **65**(11), 1337–1339 (1994).
27. M. Grabherr, R. Jager, M. Miller, C. Thalmaier, J. Herlein, R. Michalzik, and K. J. Ebeling, “Bottom-emitting VCSEL's for high-CW optical output power,” IEEE Photon. Technol. Lett. **10**(8), 1061–1063 (1998).
28. Y.-K. Kuo, J.-R. Chen, M.-Y. Jow, C.-Z. Wu, B.-J. Pong, and C.-C. Chen, “Optimization of oxide-confinement and active layers for high-speed 850-nm VCSELs,” Proc. SPIE **6132**, 61320M (2006).
29. L. Solymar and D. Walsh, *Lectures on the Electrical Properties of Materials* (Oxford University Press, 1985).
30. C.-F. Hsu, P. S. Zory, C.-H. Wu, and M. A. Emanuel, “Coulomb enhancement in InGaAs-GaAs quantum-well lasers,” IEEE J. Sel. Top. Quantum Electron. **3**(2), 158–165 (1997).
31. J. Piprek, Y. A. Akulova, D. I. Babic, L. A. Coldren, and J. E. Bowers, “Minimum temperature sensitivity of 1.55 μm vertical-cavity lasers at −30 nm gain offset,” Appl. Phys. Lett. **72**(15), 1814–1816 (1998).

1. Introduction

Vertical-cavity surface-emitting lasers (VCSELs) have been proved as strong competitors to edge-emitting semiconductor lasers because of its significant advantages such as circular output beam, low threshold current, low cost and easy fabrication in two-dimensional arrays to scale up the power [1–3]. These advantages, together with its high-speed modulation, have made it widespread application in short-distance parallel fiber-optic interconnects and high-power laser source [4–6]. VCSELs emitting at many different wavelengths have been extensively studied and some 980, 850, and 780 nm devices have been commercialized into various lightwave systems [7–9]. Meanwhile, blue–ultra-violet GaN, red AlGaInP, and 1300–1550 nm long-wavelength devices are now being developed and have achieved a considerable performance [8,10,11].

808 nm is a wavelength of great interest for high-power laser sources. Such laser sources are used to pump solid state lasers (Nd:YAG or Nd:YVO4) for end uses such as material cutting, light welding, marking and printing [12,13]. However, we find very few reports on 808-nm VCSELs after an extensive literature search, because it is only actively studied in recent years. VCSEL emitting at 808 +/− 1 nm is first presented in an outlook with the output power of 25 mW [14]. Also, the emitting wavelength of 803.3 nm is achieved for a VCSEL with the output power of 0.3 W [15]. In addition, the high power of more than 120 W has been demonstrated for two-dimensional VCSEL arrays emitting about 808 nm [12]. Yet, these literatures mainly discussed the fabrication and output results. Until now, to our knowledge, there is no report about the structure design and material optimization for the quantum-well active region of 808-nm VCSELs.

In this paper, we design an unstrained GaAs, a tensilely strained $GaAs_xP_{1-x}$ and a compressively strained $In_{1-x-y}Ga_xAl_yAs$ quantum-well active regions in order to emit near 808

nm at operating temperature of VCSELs. First, we present a comprehensive model for the calculation of the bulk bandgap, effective mass, band offset and critical thickness of these quantum-well systems. Then, the relationship between the emission wavelength and the width of quantum wells (QWs) with an arbitrary composition is established. Also, the PICS3D (Photonic Integrated Circuit Simulator in 3D) [16] simulation program is employed to calculate the material gain of these quantum-well systems at different temperatures with variant carrier densities. Furthermore, the threshold current density versus the number of QWs is plotted. Finally, the output power of the three designed quantum-well VCSELs is studied in considering the self-heating effect.

2. Parameters and physical model

To obtain the numerical parameters for both the $GaAs_xP_{1-x}$ and $In_{1-x-y}Ga_xAl_yAs$ material systems, a linear interpolation between the parameters of the relevant binary semiconductors is utilized except for the unstrained bandgap energies. For physical parameter P, the interpolation formulas are given as [17]

$$\mathrm{P}(\mathrm{GaAs_xP_{1\text{-}x}}) = \mathrm{P}(\mathrm{GaAs})x + \mathrm{P}(\mathrm{GaP})(1-x), \tag{1}$$

$$\mathrm{P}(\mathrm{In_{1\text{-}x\text{-}y}Ga_xAl_yAs}) = \mathrm{P}(\mathrm{InAs})(1-x-y) + \mathrm{P}(\mathrm{GaAs})x + \mathrm{P}(\mathrm{AlAs})y. \tag{2}$$

Table 1. Parameters of the Binary Semiconductors Used in this Study

Parameter	Symbol (unit)	GaAs	GaP	InAs	AlAs
Lattice constant	a (Å)	5.6533	5.4505	6.0584	5.660
Hydrostatic deformation potential					
for conduction band	a_c (eV)	−7.17	−7.14	−5.08	−5.64
for valence band	a_v (eV)	1.16	1.70	1.00	2.47
Elastic stiffness constants	C_{11} (10^{11}dyn/cm^2)	11.879	14.05	8.329	12.5
Elastic stiffness constants	C_{12} (10^{11}dyn/cm^2)	5.376	6.203	4.526	5.34
Shear deformation potential	b (eV)	−1.7	−1.8	−1.8	−1.5
Luttinger parameters	γ_1	6.8	4.05	20.4	3.45
	γ_2	1.9	0.49	8.3	0.68
	γ_3	2.73	1.25	9.1	1.29
Electron effective mass	m_e/m_0	0.067	0.25	0.023	0.15
Heavy-hole effective mass	m_{hh}/m_0	0.50	0.67	0.40	0.79
Average valence band position	$E_{v,av}$ (V)	−6.92	−7.40	−6.67	−7.49
Spin-orbit split-off energy	Δ (V)	0.34	0.08	0.38	0.28
Thermal conductivity	λ_c (W/cm·K)	0.45	0.77	0.3	0.91

The material parameters of the binary semiconductors [17–19] can be found in Table 1. From Eqs. (1) and (2), we can obtain most physical parameters for GaAsP and InGaAlAs in the calculation, and the exceptional unstrained bandgap energies are calculated by following expressions

$$E_{g0}(\mathrm{GaAs_xP_{1\text{-}x}}) = 2.75 - 1.54x + 0.21x^2\mathrm{eV}, \tag{3}$$

$$\begin{aligned} E_{g0}(\mathrm{In_{1\text{-}x\text{-}y}Ga_xAl_yAs}) = {} & 0.36 + 2.093y + 0.629x + 0.577y^2 + 0.436x^2 \\ & + 1.013xy - 2.0xy(1-x-y)\mathrm{eV}. \end{aligned} \tag{4}$$

2.1 Impact of strain on quantum-well band

Based on the strain theory [20,21], the bulk bandgap of strained quantum well is calculated. In the case of (001) oriented (z axis) growth, the strain has the following components:

$$\varepsilon = \varepsilon_{xx} = \varepsilon_{yy} = \frac{a_0 - a}{a}, \tag{5}$$

#146072 - $15.00 USD Received 18 Apr 2011; accepted 1 Jun 2011; published 14 Jun 2011
(C) 2011 OSA

$$\varepsilon_{zz} = -\frac{C_{12}}{C_{11}}(\varepsilon_{xx} + \varepsilon_{yy}) = -2\frac{C_{12}}{C_{11}}\varepsilon. \tag{6}$$

where a is the lattice constant of the quantum well, a_0 is the lattice constant of the substrate, C_{11} and C_{12} are the elastic stiffness constants. For the quantum well layer, the conduction band is shifted by the energy

$$\delta E_c = a_c(\varepsilon_{xx} + \varepsilon_{yy} + \varepsilon_{zz}), \tag{7}$$

and the valence bands are shifted by

$$\delta E_{lh} = \mathrm{a}_v(\varepsilon_{xx} + \varepsilon_{yy} + \varepsilon_{zz}) - \frac{b}{2}(\varepsilon_{xx} + \varepsilon_{yy} - 2\varepsilon_{zz}), \tag{8}$$

$$\delta E_{hh} = \mathrm{a}_v(\varepsilon_{xx} + \varepsilon_{yy} + \varepsilon_{zz}) + \frac{b}{2}(\varepsilon_{xx} + \varepsilon_{yy} - 2\varepsilon_{zz}), \tag{9}$$

where a_c and a_v are the conduction-band and valence-band hydrostatic deformation potentials, and b is the valence-band shear deformation potential.

For tensilely strained $GaAs_xP_{1-x}$ and compressively strained $In_{1-x-y}Ga_xAl_yAs$ material systems, the strained bandgaps can be expressed as

$$E_{c-lh}(\mathrm{GaAsP}) = E_{g0}(x) + \delta E_c - \delta E_{lh}, \tag{10}$$

$$E_{c-hh}(\mathrm{InGaAlAs}) = E_{g0}(x, y) + \delta E_c - \delta E_{hh}, \tag{11}$$

where E_{g0} can be gotten from Eqs. (3) and (4), δE_c, δE_{lh}, and δE_{hh} can be respectively gotten by substituting Eqs. (5) and (6) into Eqs. (7), (8) and (9).

During the calculation of the energy levels in the valence band of strained quantum well, the hole effective mass can be taken as

$$m_z = \begin{cases} 1/(\gamma_1 + 2\gamma_2), & (for \quad light \quad hole) \\ 1/(\gamma_1 - 2\gamma_2), & (for \quad heavy \quad hole) \end{cases}. \tag{12}$$

2.2 Band offset

The band offset is the relative position of the band edges of the semiconductors constituting the QW. There are few experimental data for the band offsets of these strained semiconductor alloys with various compositions, so the theoretical model for the calculation of the conduction and valence band edges become important in designing and modeling stages. Here we present model-solid theory [17,18] for the band alignment of these systems.

The valence band position of potential well is given by

$$E_v = \begin{cases} E_{v,av} + \frac{\Delta}{3} + \delta E_{lh}, (tensile \quad strain) \\ E_{v,av} + \frac{\Delta}{3} + \delta E_{hh}, (compressive \quad strain) \end{cases}, \tag{13}$$

where $E_{v,av}$ is the average valence subband energy and Δ is the spin-orbit split-off band energy. The conduction band position may be calculated by simply adding the strained bandgap energy to the valence band position. Then the band offset ratio of the conduction can be given by

$$\mathrm{Q_c} = \frac{\Delta E_c}{\Delta E_g} = 1 - \frac{E_v^w - E_v^b}{E_g^b - E_g^w}, \tag{14}$$

where Ew v and Eb v obtained by Eq. (13) are respectively the valence band position in the potential well and potential barrier materials, and Ew g and Eb g respectively correspond to the strain adjusted band gaps for the potential well and potential barrier materials.

2.3 Critical thickness

To the strained material of lattice mismatched system, the maximum thickness h_c must be taken into account in order not to cause misfit dislocation. If the epitaxial layer is thin enough, as well as the mismatch rate is not more than 7-9%, the system can maintain the energy of elastic strain is less than the energy in forming dislocation. By using mechanical equilibrium model, Matthews gives the expression for the critical thickness h_c as [22]

$$h_c = \frac{a\left[1-\frac{C_{12}}{4(C_{11}+C_{12})}\right]}{\kappa\sqrt{2}\pi\varepsilon(1+\frac{C_{12}}{C_{11}+C_{12}})}\left[\ln(\frac{\sqrt{2}h_c}{a}+1)\right], \quad (15)$$

where κ is the constant whose value is 1, 2 or 3 respectively corresponding to the strain superlattice, MQW, or single strained layer.

2.4 Output power

Table 2. Parameters Used in the Calculation of Output Power

Parameter	Symbol (unit)	Value
Reflectivity	R (%)	99.4
Effective cavity length	L (nm)	960
Total internal loss	α_{in} (cm^{-1})	15
Internal quantum efficiency	η_i (%)	100
Cutoff temperature	T_{off} (°C)	170
The turn-on voltage	V_0 (V)	1.5
Series resistance	R_d (Ω)	6
Effective recombination constant	B_{eff} (cm^3/s)	1.5×10^{-10}
Gain coefficient		
for GaAs 4 nm	a_N (cm^{-1})	4500
for $GaAs_{0.87}P_{0.13}$ 13 nm	a_N (cm^{-1})	2000
for $In_{0.14}Ga_{0.74}Al_{0.12}As$ 6 nm	a_N (cm^{-1})	3900
Transparency carrier concentration		
for GaAs	N_t (cm^3)	3.5×10^{18}
for $GaAs_{0.87}P_{0.13}$	N_t (cm^3)	1.5×10^{18}
for $In_{0.14}Ga_{0.74}Al_{0.12}As$	N_t (cm^3)	1.8×10^{18}

For the uniform gain structure (UGS) VCSEL with quantum-well active layer, the threshold current can be written as [23]

$$I_{th} = I_s \exp(\frac{2}{a_N n_w L_w}[\alpha_{in} L + \log(\frac{1}{R})]), \quad (16)$$

where

$$I_s = q n_w L_w B_{beff} N_t^2 \pi r^2, \quad (17)$$

where n_w and L_w are respectively the number and width of QWs, r and R are respectively the radius and reflectivity of VCSEL, B_{eff} is the effective recombination constant, L is the effective cavity length, α_{in} is the total internal loss, a_N is the gain coefficient, and N_t is the carrier concentration at transparency. The differential quantum efficiency can be written as [24,25]

$$\eta_d = \eta_i \frac{\log(1/R)}{\alpha_{in} L + \log(1/R)}, \tag{18}$$

where η_i is the internal quantum efficiency. Considering the self-heating effect of VCSEL [26], the experience formula of the device output power can be expressed as [23,27]

$$P = \frac{h\nu}{q}(I - I_{th})\eta_d(1 - \frac{\Delta T}{T_{off}}), \tag{19}$$

where

$$\Delta T = [(V_0 + IR_d)I - P]/(4\lambda_c r), \tag{20}$$

where T_{off} is the cutoff temperature, R_d is the series resistance, V_0 is the turn-on voltage, I is the injection current, and λ_c is the thermal conductivity listed in Table 1. The other parameters used in the calculation of output power can be found in Table 2 [12,23]. It should be noted that the gain coefficient and the transparency carrier concentration are obtained by PICS3D simulator.

3. Results and discussion

In order to investigate the effect of strain on InGaAlAs QWs, we did an extensive literature search to find that the strain of InGaAlAs when less than 1.5% is the bigger the better [28]. However, the early epitaxial process indicated the epitaxial nucleation on the substrate is very difficult when the lattice mismatch of the two materials is more than 1%. Based on these two points, we determine the In content of InGaAlAs 0.14. In this case, the strain of InGaAlAs is about 1% with the critical value of nucleation.

Table 3. Theoretical Results of Effective Mass, Strain, Bulk Bandgap, Band Offset and Critical Thickness

Material	m_e/m_0	m_v/m_0	ε (%)	E_g (eV)	ΔE_c (eV)	ΔE_v (eV)	h_c (nm)
$Al_{0.3}Ga_{0.7}As$[a]	0.0919	0.5870[a]	0	1.7981			
GaAs	0.0670	0.5000	0	1.4240	0.19827	0.17583	
$GaAs_{0.85}P_{0.15}$	0.0945	0.1024	0.541	1.5251	0.15596	0.11704	47.62
$GaAs_{0.86}P_{0.14}$	0.0926	0.1018	0.505	1.5179	0.15924	0.12096	51.80
$GaAs_{0.87}P_{0.13}$	0.0908	0.1013	0.469	1.5107	0.16247	0.12493	56.67
$In_{0.14}Ga_{0.75}Al_{0.11}As$	0.0700	0.3320	1.006	1.4291	0.20136	0.16764	22.48
$In_{0.14}Ga_{0.74}Al_{0.12}As$	0.0708	0.3330	1.007	1.4433	0.19322	0.16158	22.45
$In_{0.14}Ga_{0.73}Al_{0.13}As$	0.0716	0.3340	1.008	1.4576	0.18503	0.15547	22.42
$In_{0.14}Ga_{0.72}Al_{0.14}As$	0.0725	0.3351	1.009	1.4719	0.17680	0.14940	22.40
$In_{0.14}Ga_{0.71}Al_{0.15}As$	0.0733	0.3361	1.010	1.4863	0.16847	0.14333	22.36

[a] $Al_{0.3}Ga_{0.7}As$ is the potential barrier whose hole effective mass 0.587 is obtained by interpolation and used in the case of no strain. When $Al_{0.3}Ga_{0.7}As$ acts as the strained potential barrier, its value is 0.3667 obtained through Eq. (12).

Applying Eq. (1) to Eq. (15), we theoretically calculate the effective mass, strain, bulk bandgap, band offset and critical thickness of unstrained GaAs, tensilely strained $GaAs_xP_{1-x}$ and compressively strained $In_{1-x-y}Ga_xAl_yAs$ quantum-well systems. The calculation results are listed in Table 3. As can be seen, the compressively strained InGaAlAs has larger band offset than the tensilely strained GaAsP, which predicts to result in better carrier confinement in InGaAlAs quantum-well system [17].

3.1 Energy levels

In the quantum well structure, the energy levels of square potential well can be estimated by the Kronig-Penney Model, and the distribution of energy levels can be gotten from the following equation [29]

$$\cos(k(L_w + L_b)) = \cos(k_b L_b)\cos(k_w L_w) - \frac{k_w^2 + k_b^2}{2k_w k_b}\sin(k_b L_b)\sin(k_w L_w), \quad (21)$$

where

$$k_b = i\sqrt{2m_b(V-E)}\Big/\hbar, \qquad k_w = \sqrt{2m_w E}\Big/\hbar, \quad (22)$$

where L_w and L_b are respectively the width of potential well and potential barrier, m_w and m_b are respectively the effective mass of potential well and potential barrier, V is the band offset of the conduction band or valence band, and E is the energy level.

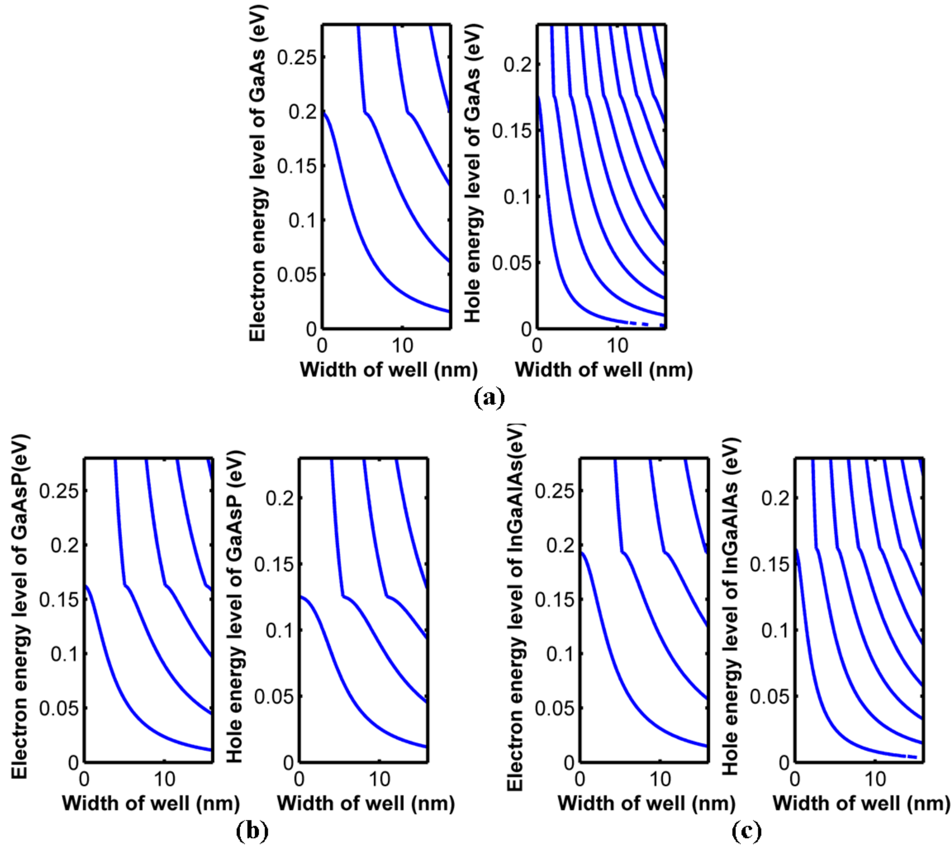

Fig. 1. Energy levels of (a) unstrained GaAs well, (b) tensilely strained $GaAs_{0.87}P_{0.13}$ well, and (c) compressively strained $In_{0.14}Ga_{0.74}Al_{0.12}As$ well with the $Al_{0.3}Ga_{0.7}As$ barrier.

After the calculations of band offset and effective mass listed in Table 3, the relationship between the quantum energy levels and the quantum-well width can be obtained by substituting Eq. (22) into Eq. (21). The simulation shows that the energy level diagrams of InGaAlAs with different compositions are similar, so we only list a representative case. Figure 1 shows the energy levels of (a) the unstrained GaAs, (b) the tensilely strained $GaAs_{0.87}P_{0.13}$, and (c) the compressively strained $In_{0.14}Ga_{0.74}Al_{0.12}As$ potential wells with the $Al_{0.3}Ga_{0.7}As$ barrier as a function of well width. In these three sub-graphs, the left one of each graph is the electronic energy levels which are calculated from the bottom of the conduction band, and the right one is the hole energy levels which are calculated from the top of the valence band. We can see that the hole energy levels of the unstrained GaAs is the most compact as shown in Fig. 1(a), while the tensilely strained GaAsP is the most decentralized as shown in Fig. 1(b),

and the compressively strained InGaAlAs has a moderate situation as shown in Fig. 1(c). The first hole subband is the heavy hole band for the unstrained GaAs and the compressively strained InGaAlAs wells, while it is the light hole band for the tensilely strained GaAsP well.

3.2 Emission wavelength

The emission wavelength of semiconductor quantum-well lasers is mainly determined by the transitions between the first subband electrons in the conduction band and the first subband holes in the valence band. The photon energy of transitions can be expressed as [30]

$$E = \frac{hc}{\lambda} = \begin{cases} E_g + E_{c1} + E_{v1} \\ E_{c-lh} + E_{c1} + E_{lh1}, \\ E_{c-hh} + E_{c1} + E_{hh1} \end{cases} \tag{23}$$

where $E_{c\text{-}lh}$ and $E_{c\text{-}hh}$ can be respectively gotten from Eqs. (10) and (11), and E_{c1}, E_{v1}, E_{lh1} and E_{hh1} can be gotten from Eq. (21).

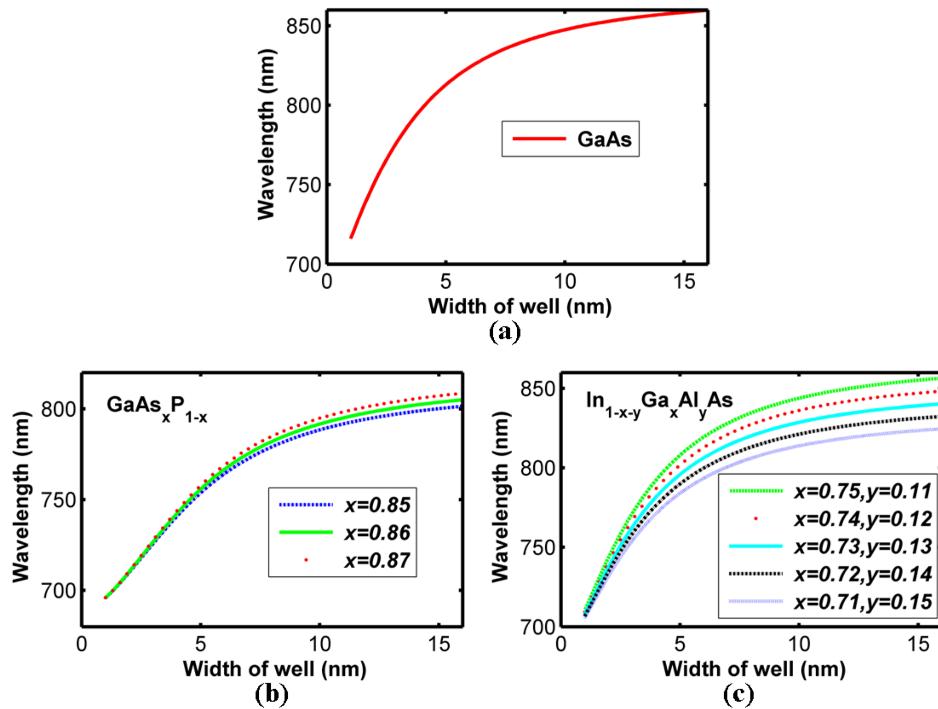

Fig. 2. Emission wavelength of (a) unstrained GaAs well, (b) tensilely strained GaAsP well, and (c) compressively strained InGaAlAs well with the $Al_{0.3}Ga_{0.7}As$ barrier.

By solving Eq. (23), we determine the composition and width of these three quantum wells under the condition of emitting a particular wavelength. Figure 2 plots the emission wavelength of (a) the unstrained GaAs, (b) the tensilely strained GaAsP, and (c) the compressively strained InGaAlAs potential wells with the $Al_{0.3}Ga_{0.7}As$ barrier as a function of well width. Because the emission wavelength becomes red shifted with the increasing temperature of active region [26,31], the wavelength of our designed VCSELs should be about 800 nm at room temperature in order to emit about 808 nm at operating temperature. Taking into account the thickness error by MOCVD growth, the width of QWs should be taken as integer nanometer. Based on these two points, we can obtain the width of GaAs, $In_{0.14}Ga_{0.74}Al_{0.12}As$, $In_{0.14}Ga_{0.72}Al_{0.14}As$, and $In_{0.14}Ga_{0.71}Al_{0.15}As$ wells is respectively 4 nm, 5 nm, 6 nm, and 7 nm with the emission wavelength of 800 nm as shown in Fig. 2(a) and Fig.

#146072 - $15.00 USD
Received 18 Apr 2011; accepted 1 Jun 2011; published 14 Jun 2011
(C) 2011 OSA

2(c). When the mismatch is less than 0.5%, the growth quality of materials will be good. Thus, we tend to select $GaAs_{0.87}P_{0.13}$ as potential well because its strain is just less than 0.5% as seen in Table 3. In addition, its width is 12 nm with the emission wavelength of 800 nm as shown in Fig. 2(b).

3.3 Material gain

The material gain is defined as the ratio of the additional photon flux to the total photon flux in per unit length. The gain spectral function can be expressed as [30]

$$g_0(E_{cv}) = \frac{\pi e^2 \hbar}{\varepsilon_0 c^3 m_0^2 n_{av}} \sum_{j,i} (1/E_{cv}) \left| M_{ji}(E_{cv}) \right|^2 \rho_{r,ji} \left[f_e(E_{cjk} + f_n(E_{vjk}) - 1) \right], \quad (24)$$

where $|M_{ji}(E_{cv})|^2$ is the transition matrix element at transition energy E_{cv}, $\rho_{r,ji}$ is the reduced density of states, n_{av} is the background refractive index. Based on Eq. (24), the material gain is calculated in the PICS3D software.

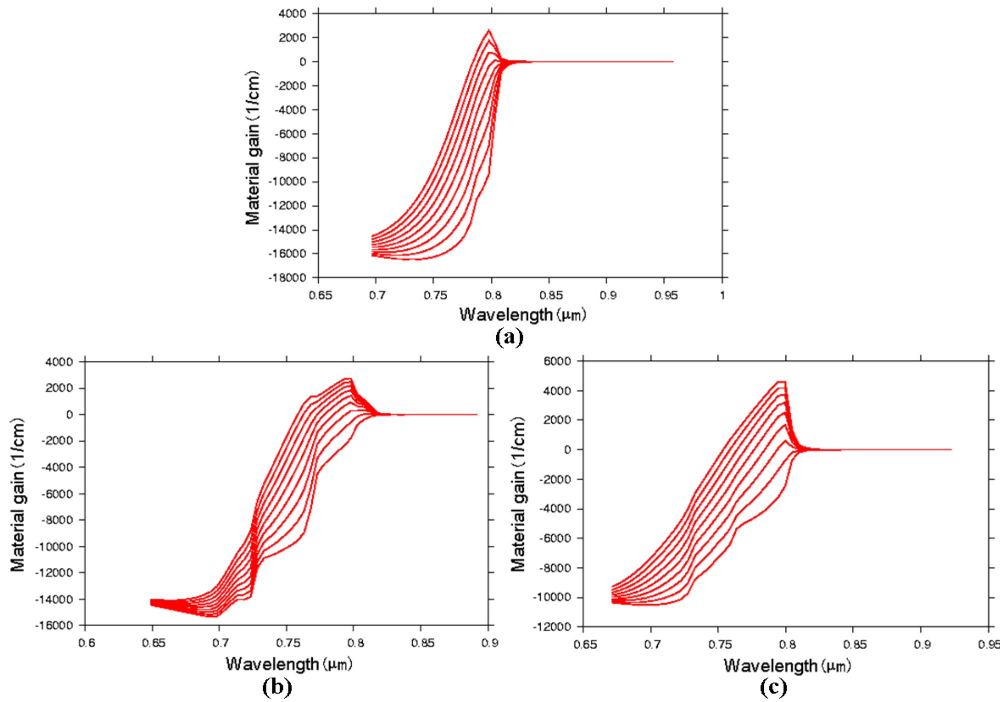

Fig. 3. Material gain of (a) unstrained GaAs well with width of 4nm and $Al_{0.3}Ga_{0.7}As$ barrier, (b) tensilely strained $GaAs_{0.87}P_{0.13}$ well with width of 13nm and $Al_{0.3}Ga_{0.7}As$ barrier, and (c) compressively strained $In_{0.14}Ga_{0.74}Al_{0.12}As$ well with width of 6nm and $Al_{0.3}Ga_{0.7}As$ barrier.

After many simulation tests, we found that the gain peak wavelength of the unstrained GaAs well with width of 4 nm, the tensilely strained $GaAs_{0.87}P_{0.13}$ well with width of 13 nm and the compressively strained $In_{0.14}Ga_{0.74}Al_{0.12}As$ well with width of 6 nm is just near 800 nm at 300 K. Figure 3 shows the simulation results which are basically consistent with the theoretical results. The injection carrier density linearly changes from 1×10^{18} cm^3 to 5×10^{18} cm^3, and the material gain increases with the increase of the injection carrier density. As can be seen, the compressively strained $In_{0.14}Ga_{0.74}Al_{0.12}As$ has the highest peak material gain as shown in Fig. 3(c), while the unstrained GaAs has the lowest value as shown in Fig. 3(a), and the tensilely strained $GaAs_{0.87}P_{0.13}$ has a moderate value as shown in Fig. 3(b).

#146072 - $15.00 USD Received 18 Apr 2011; accepted 1 Jun 2011; published 14 Jun 2011
(C) 2011 OSA

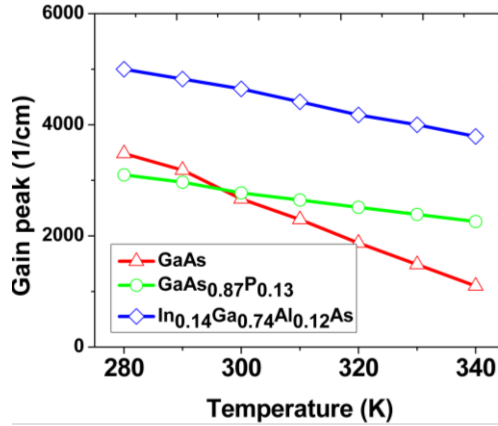

Fig. 4. Peak material gain versus operating temperature for the three QWs.

To explore the effect of temperature on the peak material gain, we will discuss the gain peak of the three QWs described in Fig. 3. When the injection carrier density is 5×10^{18} cm^3, the peak material gain versus operating temperature for GaAs well with width of 4 nm, $GaAs_{0.87}P_{0.13}$ well with width of 13 nm and $In_{0.14}Ga_{0.74}Al_{0.12}As$ well with width of 6 nm is plotted in Fig. 4. It is shown that $GaAs_{0.87}P_{0.13}$ has the lowest peak material gain when the operating temperature is smaller than 295 K, while GaAs has the lowest value when the operating temperature is bigger than 295 K. We can also see that the tensilely strained $GaAs_{0.87}P_{0.13}$ has the best temperature stability of the peak material gain, while the unstrained GaAs has the worst, and the compressively strained $In_{0.14}Ga_{0.74}Al_{0.12}As$ has a moderate value. In particular, the compressively strained $In_{0.14}Ga_{0.74}Al_{0.12}As$ has the highest peak material gain at all operating temperature.

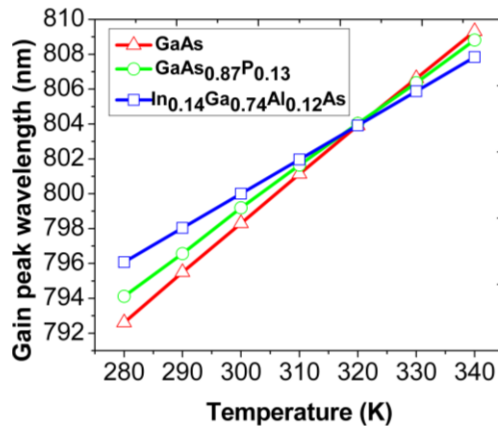

Fig. 5. Gain peak wavelength versus operating temperature for the three QWs.

When the injection carrier density is 5×10^{18} cm^3, the gain peak wavelength versus operating temperature for the three QWs is plotted in Fig. 5. As can be seen, the gain peak wavelength becomes red shifted with the increase of temperature. At 300K, the gain peak wavelength of the three QWs is near 800 nm as described in Fig. 3. The working temperature of VCSELs is about 30-40 K higher than the room temperature [26]. At this time, the gain peak wavelength of these three QWs is near 808 nm as shown in Fig. 5. We can also see that the gain peak wavelength shift with temperature for the $GaAs/Al_{0.3}Ga_{0.7}As$ QW is about 0.278 nm/K, while for the $GaAs_{0.87}P_{0.13}/Al_{0.3}Ga_{0.7}As$ QW, it is about 0.245 nm/K, and for the

$In_{0.14}Ga_{0.74}Al_{0.12}As/Al_{0.3}Ga_{0.7}As$ QW, it is about 0.196 nm/K. That is to say, the compressively strained $In_{0.14}Ga_{0.74}Al_{0.12}As$ has the best temperature stability of gain peak wavelength.

3.4 Output characteristics

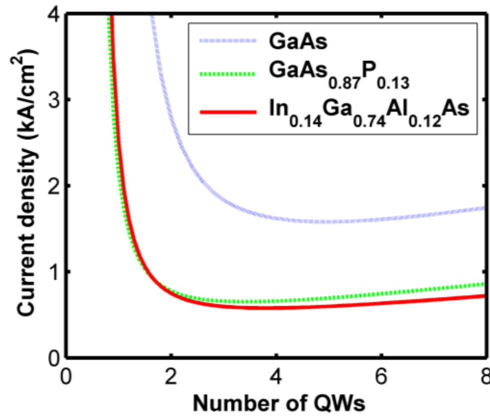

Fig. 6. Threshold current density of the unstrained GaAs, the tensilely strained $GaAs_{0.87}P_{0.13}$ and the compressively strained $In_{0.14}Ga_{0.74}Al_{0.12}As$ quantum-well VCSELs.

The threshold current density of the three designed quantum-well VCSELs can be obtained by substituting Eq. (17) divided by the area into Eq. (19), and the parameters used in the calculation can be found in Table 2. Figure 6 shows the threshold current density versus the number of the three QWs described in Fig. 3. As can be seen, the threshold current density decreases first and then increases with the increase of the number of QWs. When the number of QWs is three, the $GaAs_{0.87}P_{0.13}$ and $In_{0.14}Ga_{0.74}Al_{0.12}As$ quantum-well VCSELs have the lowest threshold current density. Meanwhile, the total thickness of these two QWs is smaller than the critical thickness listed in Table 3. When the number of QWs is four, the GaAs quantum-well VCSEL has the lowest threshold current density. In order to compare, we also choose the number of GaAs QWs three. At this time, the compressively strained $In_{0.14}Ga_{0.74}Al_{0.12}As$ quantum-well VCSEL has the lowest threshold current density, while the unstrained GaAs has the highest, and the tensilely strained $GaAs_{0.87}P_{0.13}$ has a moderate value which is a little higher than the lowest point.

Table 4. Detailed Information for the Structure of Each Active Region

Layer	Structure (1)	Structure (2)	Structure (3)
P-spacer	Gradual $Al_xGa_{1-x}As$ 104nm	Gradual $Al_xGa_{1-x}As$ 86nm	Gradual $Al_xGa_{1-x}As$ 98nm
Barrier[a]	$Al_{0.3}Ga_{0.7}As$ 5nm	$Al_{0.3}Ga_{0.7}As$ 8nm	$Al_{0.3}Ga_{0.7}As$ 8nm
Potential well[b]	GaAs 4nm	$GaAs_{0.87}P_{0.13}$ 13nm	$In_{0.14}Ga_{0.74}Al_{0.12}As$ 6nm
Barrier	$Al_{0.3}Ga_{0.7}As$ 5nm	$Al_{0.3}Ga_{0.7}As$ 8nm	$Al_{0.3}Ga_{0.7}As$ 8nm
N-spacer	Gradual $Al_xGa_{1-x}As$ 104nm	Gradual $Al_xGa_{1-x}As$ 86nm	Gradual $Al_xGa_{1-x}As$ 98nm

[a]Barrier next to the p-spacer is grown by three times.
[b]Potential well is grown by three times.

So far, we can present the structure of these three quantum-well active regions of 808-nm VCSELs and Table 4 shows the detailed information. The AlGaAs spacer layers are employed so that the cavity is one wavelength in length. The Al content of gradual layer linearly changes from 0.3 to 0.6, which can limit the carriers and reduce the series resistance at the same time.

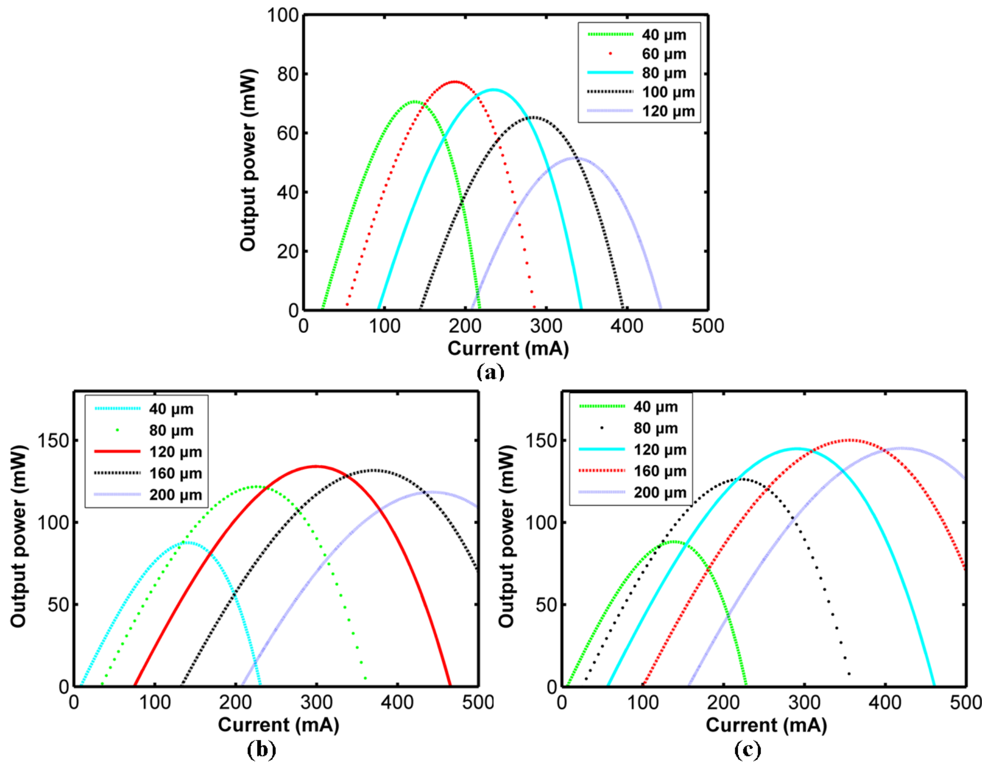

Fig. 7. Output power of (a) unstrained GaAs, (b) tensilely strained $GaAs_{0.87}P_{0.13}$, and (c) compressively strained $In_{0.14}Ga_{0.74}Al_{0.12}As$ quantum-well VCSELs with different apertures.

Considering the self-heating effect, the device output power can be obtained by substituting Eqs. (16), (17), (18) and (20) into Eq. (19). Figure 7 shows the relationship between the output power and the injection current under different apertures of the three designed quantum-well VCSELs. The injection current linearly changes from 0 to 500 mA. As can be seen, the output power increases first and then decreases with the increase of the injection current, which can be attributed to the self-heating effect of VCSELs. At the same time, the output power varies with the aperture size of VCSELs. The maximum output power of GaAs quantum-well VCSEL is next to 80 mW when the device diameter is 60 µm as shown in Fig. 7(a), while for $GaAs_{0.87}P_{0.13}$ quantum-well VCSEL, it is next to 140 mW when the device diameter is 120 µm as shown in Fig. 7(b), and for $In_{0.14}Ga_{0.74}Al_{0.12}As$ quantum-well VCSEL, it exceeds 150 mW when the device diameter is 160 µm as shown in Fig. 7(c).Thus, we can draw that the $In_{0.14}Ga_{0.74}Al_{0.12}As$ quantum-well VCSEL has the largest output power. When the aperture is 80 µm, the slope efficiency of GaAs quantum-well VCSEL is about 57% as shown in Fig. 7(a), while for $GaAs_{0.87}P_{0.13}$ quantum-well VCSEL, it is about 60% as shown in Fig. 7(b), and for $In_{0.14}Ga_{0.74}Al_{0.12}As$ quantum-well VCSEL, it is about 65% as shown in Fig. 7(c). Thus, we can draw that the $In_{0.14}Ga_{0.74}Al_{0.12}As$ quantum-well VCSEL has the largest slope efficiency. It is also shown that when the aperture size is the same, the $In_{0.14}Ga_{0.74}Al_{0.12}As$ quantum-well VCSEL has the lowest threshold current, while the GaAs quantum-well VCSEL has the highest, and the $GaAs_{0.87}P_{0.13}$ quantum-well VCSEL has a moderate value. This result is consistent with the result described in Fig. 6.

4. Conclusion

An unstrained $GaAs/Al_{0.3}Ga_{0.7}As$, a tensilely strained $GaAs_xP_{1-x}/Al_{0.3}Ga_{0.7}As$ and a compressively strained $In_{1-x-y}Ga_xAl_yAs/Al_{0.3}Ga_{0.7}As$ quantum-well active regions are designed in order to emit near 808 nm at operating temperature of VCSELs. The numerical simulation

#146072 - $15.00 USD Received 18 Apr 2011; accepted 1 Jun 2011; published 14 Jun 2011
(C) 2011 OSA

shows that the gain peak wavelength is near 800 nm at room temperature for GaAs well with width of 4 nm, $GaAs_{0.87}P_{0.13}$ well with width of 13 nm and $In_{0.14}Ga_{0.74}Al_{0.12}As$ well with width of 6 nm. Furthermore, the output characteristics of the three designed quantum-well VCSELs are studied and compared. The number of QWs is chosen three due to the lowest threshold current density. The maximum output power of $In_{0.14}Ga_{0.74}Al_{0.12}As$ quantum-well VCSEL exceeds 150 mW when the device diameter is 160 µm, while for $GaAs_{0.87}P_{0.13}$ quantum-well VCSEL, it is next to 140 mW when the device diameter is 120 µm, and for GaAs quantum-well VCSEL, it is next to 80 mW when the device diameter is 60 µm. The simulations indicate that the compressively strained $In_{0.14}Ga_{0.74}Al_{0.12}As$ is the most appropriate candidate for the quantum well of 808-nm VCSELs due to its better carrier confinement, higher temperature stability, the lowest threshold current density, and the highest material gain, slope efficiency and output power.

Acknowledgment

This work is supported by the National Natural Science Foundation of China (NNSFC) under Grant No. 60636020, 60706007, 10974012, 60876036, 90923037, 11074247, and 61006054.

#146072 - $15.00 USD Received 18 Apr 2011; accepted 1 Jun 2011; published 14 Jun 2011
(C) 2011 OSA